Numerical simulations of the latest caldera-forming eruption of Okmok volcano, Alaska

Alain Burgisser, Ally Peccia, Terry Plank, Yves Moussallam

Numerical simulations of the latest caldera-forming eruption of Okmok volcano, Alaska

Alain BURGISSER [1*], Ally PECCIA [2], Terry PLANK [2], Yves MOUSSALLAM [2]

[1] Univ. Grenoble Alpes, Univ. Savoie Mont Blanc, CNRS, IRD, Univ. Gustave Eiffel, ISTerre, 38000 Grenoble, France.

[2] Lamont-Doherty Earth Observatory, Palisades, NY 10964, USA.

* Corresponding author: Phone: (+33) 479 758 705. Email: alain.burgisser@univ-smb.fr

Abstract

The latest caldera-forming eruption of Okmok volcano, Alaska, had a global atmospheric impact with tephra deposits found in distant Arctic ice cores and a sulfate signal found in Antarctic ice cores. The associated large-scale climate cooling was driven by the amount of sulfur injected into the stratosphere during the climactic phase of the eruption. This phase was dominated by pyroclastic density currents, which have complex emplacement dynamics precluding direct estimates of the sulfur stratospheric load. We simulated the dynamics of this climactic phase with the two-phase flow model MFIX-TFM under axisymmetric conditions with several combinations of injection mass flux, emission duration, and topography. Results suggest that a steady mass flux of $8.6–28\times10^9$ kg/s is consistent with field observations. Stratospheric injections occur in pulses issued from 1) the central plume initially rising above the caldera center, 2) successive co-ignimbrite clouds caused by the encounter of the pyroclastic density currents with topography, and 3) the buoyant lift-off of dilute parts of the currents at the end of the eruption. Overall, 2.5 to 25% of the emitted volcanic gas reaches the stratosphere if the mass flux at the vent is steady. A fluctuating emission rate or an efficient final lift-off due to seawater interaction were unlikely to have increased this loading. Combined with petrological estimates of the degassed S, our results suggest that the eruption emitted 46.5–60.4 Tg S into the troposphere and injected 1.6–15.5 Tg S into the stratosphere, which controlled the atmospheric forcing and the subsequent climate response.

Keywords: pyroclastic density current, two-phase flow, sulfur, stratosphere.

1. Introduction

There is a renewed interest in the 43 BC caldera-forming eruption of Okmok volcano on the Aleutian island of Umnak, Alaska (Burgisser, 2005; Larsen et al., 2007), because its tephra deposits were found in distant Arctic ice cores and a time-correlative sulfate signal was found in Antarctic ice cores (McConnell et al. 2020; (Pearson et al. 2022). This discovery had far-reaching implications as the radiative forcing of this so-called Okmok II eruption likely caused anomalously cold years in the Northern Hemisphere, inducing inclement weather, famine, and civil unrest in the declining Roman Republic and Ptolemaic Kingdom.

The depositional sequence of the Okmok II eruption can be divided into four units of interest to establish links with the ash found in the Greenland ice core. The first unit is a deposit of silicic ash fallout (unit A1 in Burgisser, 2005) with a rhyodacitic composition (Larsen et al. 2007). The second unit is another silicic ash fallout deposits (units A2 and B1-2 in Burgisser, 2005). It is followed by a series of more mafic fallout deposits (units C1-3 in Burgisser, 2005) that are andesitic in composition (Larsen et al., 2007; Peccia et al., 2023). Finally, the fourth unit is composed of pyroclastic density current (PDC) deposits with a basaltic andesite composition that is slightly more mafic than the underlying fallout deposits (Larsen et al. 2007). The most voluminous fallout unit is the first one, but the ash found in the ice cores is not rhyodacitic; its composition matches the mafic deposits (McConnell et al. 2020). Moreover, the sulfur isotopic signature of the related sulfate signal indicates oxidation in a high-ultraviolet environment consistent with travel above the ozone layer in the lower stratosphere (McConnell et al. 2020). The third unit (and part of the second unit) is of phreatomagmatic origin due to vaporization of the pre-eruptive intracaldera lake (Burgisser, 2005). This andesitic unit has a matching composition to the Greenland ice core tephra but it only covers a small portion of Umnak Island. The corresponding plume could not have exceeded a few kms in height, making it a very unlikely candidate for stratospheric injection. Thus, the most likely culprit of the stratospheric injection is the basaltic andesitic pyroclastic density current.

Large-scale climate cooling is driven by how much sulfur was injected into the stratosphere. The eruptive phase that sent ashes to Greenland, however, deposited material from PDCs that hug topography and covered ~1000 km^2 of Umnak and the neighboring island of Unalaska (Fig. 1A). Although impressive at the regional scale, the effects of this climactic phase of the eruption are not expected to reach the high altitude required for stratospheric injection. Most of the associated volcanic sulfur, in fact, is expected to have mixed with the local atmosphere, well below the tropopause. This is because any simultaneous buoyant plume of significance would have left recognizable fall deposits interbedded with (or atop) the massive PDC deposits; this is not seen in the field (Burgisser 2005).

Quick estimates of the sulfur stratospheric load are unfortunately impossible because the dynamics of PDCs are notoriously complex. Co-ignimbrite clouds that are due to the buoyant lift off from the most dilute parts of PDCs may bring material and volcanic gases into the stratosphere (e.g., Bursik and Woods, 1991; Dufek and Bergantz, 2007a). Such clouds are generated by the complex process of partial or total gravitational collapse of the ejected material and the subsequent density stratification of the resulting PDC (e.g., Neri et al., 2007; Esposti Ongaro et al., 2020; Valentine, 2020). Estimating which fraction of pyroclasts and gas travel as PDCs and which fraction can be injected into the stratosphere from an ancient eruption is nowadays best addressed by numerical modeling.

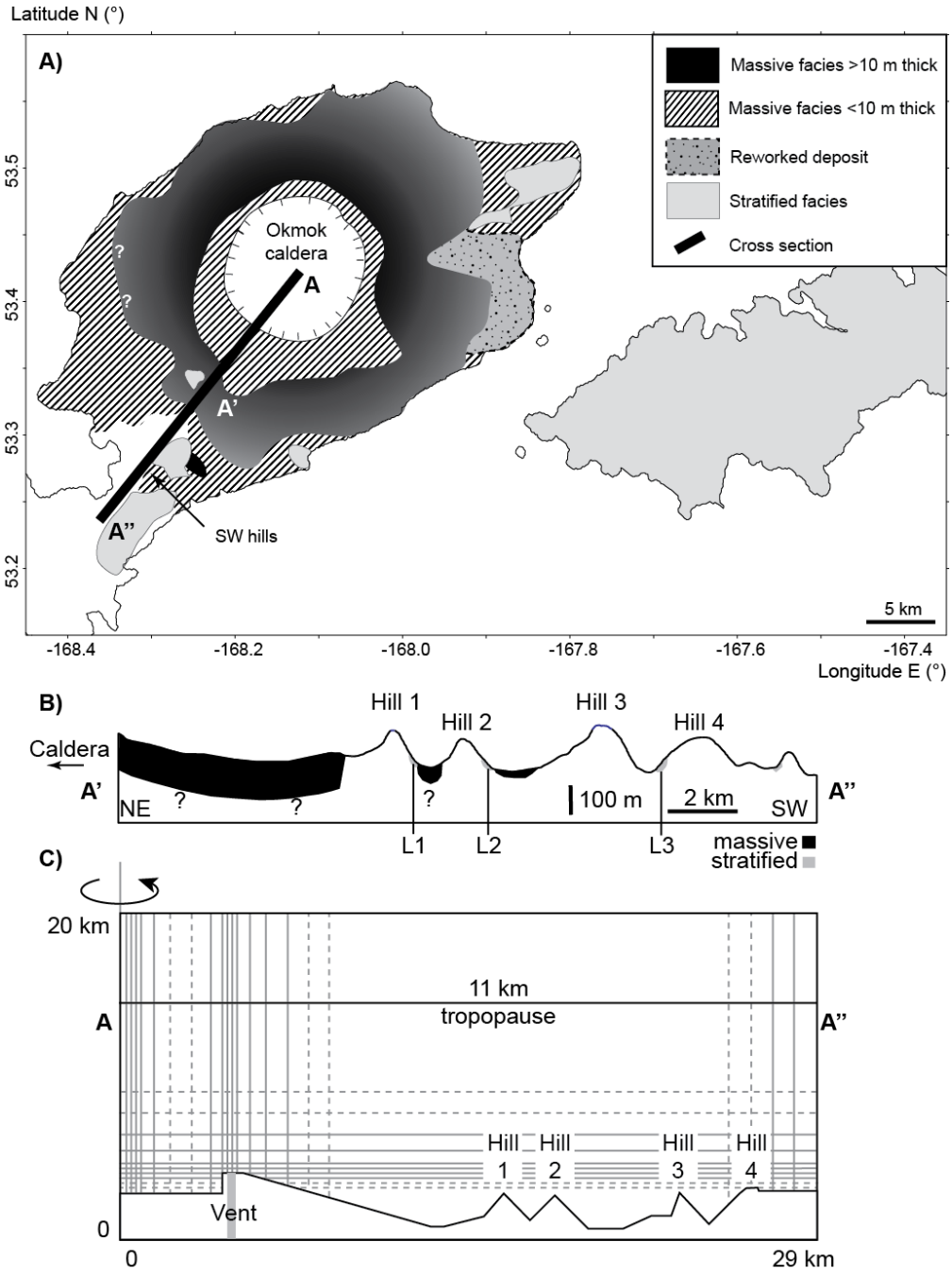

Figure 1*: Study location and simulation setup. A) Distribution of the pyroclastic deposits of the Okmok II eruption classified by broad type and thickness (modified from Burgisser, 2005). The line A–A'–A" indicates the location of the cross section shown in B) and C). B) Cross section along A'–A" with the distribution of massive and stratified deposits. Labels indicate the successive hills (Hill 1–4) that stopped the PDC as well as sampling locations (L1–3) (modified from Burgisser, 2005). C) Discretization of the axisymmetric computational domain of 20 by 29 km along the A–A" section. For clarity, the computational cells are not to scale and the topography is exaggerated vertically.*

Here we use the two-phase flow model MFIX-TFM to simulate the dynamics of the climatic phase of Okmok II eruption. MFIX-TFM has been extensively used to model volcanic flows such a

plumes and PDCs (Dufek and Bergantz, 2007a ; Dufek and Bergantz, 2007b ; Dufek et al., 2009; Benage et al., 2014 ; Benage et al., 2016; Sweeney and Valentine, 2017; Valentine and Sweeney, 2018; Breard et al., 2019; Valentine, 2020; Valentine and Cole, 2021). We mostly follow the modeling choices of Dufek and Bergantz (2007a) while incorporating more recent findings (e.g., Breard et al., 2019) to apply MFIX-TFM to the case study of Okmok II. No modeling novelty was attempted, and the dynamics of the PDC travelling over water were ignored.

The modeling was constrained by different characteristics of the deposits. The total volume of material ejected by the PDC was at least 14 km^3 Dense Rock Equivalent (DRE) (Burgisser 2005). The upper limit is far less certain, and a reasonable number based on estimates of the caldera volume (Burgisser 2005) and underwater deposits (Peccia et al. 2023) yields ~29 km^3 DRE (~50 km^3 of deposit). The nearly circular shape of the caldera and deposit componentry suggest that the collapse of the eruptive column caused the PDC to spread axisymmetrically (Burgisser 2005). The maximum PDC runout is unknown over most of the circumference of the island because no underwater data are available. One exception lies on the east, were the PDC crossed an 8-km strait to reach the neighboring island of Unalaska, where it continued its course to achieve a total runout greater than 40 km. The other exception lies on the SW of the caldera, where four successive hills located 15–25 km away from the caldera center cause deposit thickness to vanish progressively. Thick (up to 30 m), massive PDC deposits occur between the caldera rim and the first hill as well as in two shallow valleys separating the three first hills (Fig. 1B). Thin, stratified deposits are found on the upper slopes of the two first hills as well as in the two shallow valleys separating the last two hills. These stratified deposits were interpreted to result from sedimentation from dilute parts of the PDC or from the PDC head.

2. Methods

2.1. Model formulation

We performed numerical simulations by using the MFIX-TFM software (https://mfix.netl.doe.gov, v. 2016), which solves the mass, momentum, and energy balance of a mixture of gas and particles. The gas is modeled as a Newtonian fluid, the turbulence of which is represented by a k–ε model. Particles are modeled as one (or three) granular continuum with a given particle size. This combination of interpenetrating continuous phases is referred to as the Two-Fluid Model (TFM) approach. Detailed explanations about the theory and implementation of the model can be found in Garg et al. (2010), Syamlal (1998), Syamlal et al. (1993), and a validation of MFIX-TFM approach to model gas-particle flows in flumes has been done by Breard et al. (2019). Although the focus of this study is the dynamics of the mostly dilute jet, the dynamics of the dense undercurrents and the related co-ignimbrite clouds also control stratospheric injection and thus a reasonable degree of accuracy of the propagation of the dense granular flow is needed. The choices of the closure relationships thus closely follow those of Breard et al. (2019), except for the inclusion of turbulence energy dissipation (Dufek and Bergantz, 2007a).

The suspension is composed of a gas phase and m=1 to M solid phases. The conservation of mass and volume is given by:

$$\partial_t\left[\varepsilon_g\rho_g\right] + \nabla\cdot\left[\varepsilon_g\rho_g\boldsymbol{v}_g\right] = 0 \qquad (1a)$$

$$\partial_t[\varepsilon_m\rho_m] + \nabla\cdot[\varepsilon_m\rho_m\boldsymbol{v}_m] = 0 \quad (1b)$$

$$\varepsilon_g + \sum_{m=1}^{M}\varepsilon_m = \varepsilon_g + \varepsilon_b = 1 \quad (1c)$$

where ε_g is the gas volume fraction, ε_b is the sum of the volume fractions of all solid phases, ρ_g is the gas density given by the ideal gas law, $\boldsymbol{v}_g$ is the gas velocity, and ε_m, ρ_m, and $\boldsymbol{v}_m$ are the volume fraction, density, and velocity of particle phase m, respectively. The momentum conservation for the gas and the solids is:

$$\partial_t\left[\varepsilon_g\rho_g\boldsymbol{v}_g\right] + \nabla\cdot\left[\varepsilon_g\rho_g\boldsymbol{v}_g\otimes\boldsymbol{v}_g\right] + \varepsilon_g\nabla P_g + \nabla\cdot\boldsymbol{S}_g + \sum_M f_d(\boldsymbol{v}_m - \boldsymbol{v}_g) + \varepsilon_g\rho_g\boldsymbol{g} = 0 \quad (2a)$$

$$\partial_t[\varepsilon_m\rho_m\boldsymbol{v}_m] + \nabla\cdot[\varepsilon_m\rho_m\boldsymbol{v}_m\otimes\boldsymbol{v}_m] + \varepsilon_m\nabla P_g + \nabla\cdot\boldsymbol{S}_m - f_d(\boldsymbol{v}_m - \boldsymbol{v}_g) + \varepsilon_m\rho_m\boldsymbol{g} = 0 \quad (2b)$$

where P_g is the gas pressure, $\boldsymbol{g}$ is the gravity acceleration vector, $\boldsymbol{S}_g$ is the gas stress tensor, $\boldsymbol{S}_m$ is the solid stress tensor, and the drag coefficient, f_d, follows the Wen-Yu formulation (Wen and Yu 1966).

The gas stress tensor, $\boldsymbol{S}_g$, is Newtonian:

$$\boldsymbol{S}_g = -P_g\boldsymbol{I} + \boldsymbol{\tau}_g \quad (3a)$$

$$\boldsymbol{\tau}_g = 2\varepsilon_g\mu_{gt}\left(\boldsymbol{D}_g - \frac{1}{3}tr(\boldsymbol{D}_g)\boldsymbol{I}\right) \quad (3b)$$

$$\boldsymbol{D}_g = \frac{1}{2}\left[\nabla\boldsymbol{v}_g + (\nabla\boldsymbol{v}_g)^T\right] \quad (3c)$$

$$\mu_{gt} = min\left(\mu_g + 0.09\rho_g k_t^2\varepsilon_t^{-1}, 10^3\right) \quad (3d)$$

where k_t is the turbulent kinetic energy and ε_t is its rate of dissipation. A modified k–ε turbulence model suitable for dilute suspensions is used to calculate k_t and ε_t (Benyahia et al. 2005). The gas phase is assumed to be air for simplicity, although the natural eruptive gas would mostly contain water vapor and other gas species. Air viscosity, μ_g, is given by:

$$\mu_g = 1.7\times10^{-5}\left(\frac{T_g}{273}\right)^{1.5}\left(\frac{383}{T_g+110}\right) \quad (4)$$

where T_g is the gas temperature. The energy conservation for the gas and the solids reads:

$$\varepsilon_g\rho_g C_{pg}\left[\partial_t T_g + \boldsymbol{v}_g\cdot\nabla T_g\right] = \nabla\left(\kappa_g\nabla T_g\right) + \sum_M\gamma_m(T_m - T_g) \quad (5a)$$

$$\varepsilon_m\rho_m C_{pm}[\partial_t T_m + \boldsymbol{v}_m\cdot\nabla T_m] = \nabla(\kappa_m\nabla T_m) - \gamma_m(T_m - T_g) \quad (5b)$$

where C_{pg}=2200 J/kg K is the gas heat capacity, C_{pm}=1200 J/kg K is the solid heat capacity (Moitra et al. 2020), T_m is the solids temperature, γ_m is the interphase heat transfer between the solid phase m and the gas, κ_m = 2 W/K m is the solid conductivity (Moitra et al. 2020), and κ_g is the gas conductivity given by:

$$\kappa_g = 0.025\left(1 - \sqrt{1-\varepsilon_g}\right)\sqrt{\frac{T_g}{300}} \quad (6)$$

The interphase heat transfer, γ_m, is given by:

$$\gamma_m = \frac{6\kappa_g\varepsilon_m}{d_m^2}Nu_m \quad (7)$$

where Nu_m is the Nusselt number of solid phase m, which depends on the gas Prandtl number, on the particle Reynolds number, and on ε_g (Gunn 1978).

The particle stress tensor, $\boldsymbol{S}_m$, is the sum of a collisional and a frictional contribution, the full

formulation of which can be found in Benyahia (2008). Briefly, the collisional component of $\boldsymbol{S}_m$ follows the kinetic theory of granular material with a balance equation of pseudo-thermal energy describing the evolution of the granular temperature Benyahia et al., 2005; Benyahia, 2008). The particle restitution coefficient was set to 0.8. The frictional component of $\boldsymbol{S}_m$ is formulated according to the Princeton model (Benyahia, 2008), which has been shown to produce flow front velocities that are in good agreement with experimental gravity currents (Breard et al. 2019). This model calculates a solid pressure based on plastic flow theory. The friction coefficient between two particle phases was 0.5 and the angle of internal friction of the particle phases was 30°. The particle volume fraction above which friction sets in was 0.5 and the maximum packing fraction was 0.6.

Replacing the modified k–ε turbulence model by a Reynolds stress with a fixed turbulent length scale of 1 cm yielded stratospheric gas velocities in excess of 2 km/s with strong reflections of incoming pressure waves against the upper boundary throughout run duration (700 s). With the k–ε model, such pressure reflections are restricted to the first arrival of the central plume at ~100 s with gas velocities <300 m/s at the upper boundary, where the plume is very dilute and the speed of sound is close to that of a pure gas. Turbulent dissipation had thus to be taken into account to avoid unrealistically high velocities.

Burgisser (2005) used the kinematic model of Burgisser and Bergantz (2002) to derive dynamic parameters of the dilute part of the PDC from the granulometry of corresponding stratified deposits. In particular, the median particle diameter was used to deduce the root-mean-square velocity of the turbulent gas at the origin of the sedimentation of the stratified deposit, U_{rms}. The mean dilute current speed was assumed to be 4 times larger (Pope 2000). In our model, $U_{rms} = \sqrt{2k_t}$. In addition, Burgisser and Bergantz (2002) proposed that a scaling relationship established by Crowe et al. (1997) could be used to set a limit between the dense and the dilute parts within the body of a PDC. This limit is quantified by the ratio of the particle response time to the gas motion over the time between particle collision, $\left(3\mu_g f\right)/\left(\varepsilon_m \rho_p d_m V_{rms}\right)$, where V_{rms} is the root-mean-square of the particle velocity (in our model, $V_{rms} = \sqrt{3\Theta}$ with Θ the granular temperature), and f>1 is an empirical function of the particle Reynolds number (Burgisser and Bergantz 2002). The flow is dilute when this ratio is >1 and dense otherwise.

2.2. Simulation setup

The axisymmetric computational domain is depicted in Fig. 1C. Following the grid resolution of Dufek and Bergantz (2007a), it contains 354×280 cells with an edge length varying from 10 m near the ground surface, the central axis, and the vent to 100 m near the outer boundaries. A near-topography resolution of 10 m is generally considered as a good compromise to capture collapsing eruptive columns generating PDCs without excessive computational power (Valentine and Cole 2021). The domain size is 29 km wide by 20 km high except runs 6 and 7 that are 21 km wide. The atmosphere temperature was initialized according to the U.S. standard atmosphere (National Oceanic and Atmospheric Administration 1976) with the tropopause at 11 km, which is consistent with the high latitude of Okmok volcano in the summer (Liu et al. 2014). The fact that the tropopause height is a couple of kilometers lower during the winter was neglected because there is weak evidence that the climactic part of the eruption occurred before the winter months. Stratigraphic observations suggest that the ground was mostly free of snow at the time of the eruption of the two initial rhyodacitic fall deposits (Burgisser 2005). The eruption then stopped for a period of days to months before resuming by unsteady phreatomagmatic explosions followed by the caldera-forming phase of the eruption. The

consequences of this choice are probably minimal because simulations of the stratospheric injection of S from the Okmok II eruption suggest that the eruption season does not alter the climate response (Peccia et al. 2023).

Twelve runs with similar topography but varying number of particle phases, inlet mass flux and domain sizes were carried out. Two of these runs (11 and 13) were carried out with an additional scalar advection equation that tracked the amount of injected gas within the domain. That scalar, S, was used to quantify the mixing with the ambient air. Unlike temperature, which had the additional diffusion due to Fourier's law, S was only subject to numerical diffusion. In addition, one run (12) was done with a filled caldera.

The ground surface follows the topography of a rasterized DEM vertical section of Umnak Island. The DEM had a spatial resolution of 10 m (U.S. Geological Survey EROS Data Center 1999). The cross section starts from the caldera center towards a series of ~350-m-high hills on the SW of the caldera (Fig. 1A-C). The simulated topography follows that of the DEM until the top of the fourth hill at 26 km from the caldera center, after which the ground is assumed to be flat until the distal edge of the computation domain at 29 km (Fig. 1C). This edge corresponds to the position of a fifth hill that marks the maximum runout of the Okmok II PDCs (Fig. 1B). Ignoring the topography of the most distal few kilometers avoided creating a trough near the domain edge that would drive artificial vortexes influencing co-ignimbrite dynamics. Any PDC reaching past the fourth hill at 26 km was considered to be too close to the domain boundary for its distal dynamics to be properly captured. Such PDC were deemed having runouts exceeding that observed.

The boundary condition for the ground surface was that of Jenkins (1992) as implemented into MFIX-TFM by Benyahia et al. (2007). The low friction limit of this condition allows partial slip of the solids phase against the ground by particle sliding. The coefficient of restitution of the particle–ground collision was 0.7 and the angle of internal friction at the walls was set to the low value of 12°. A test run with a no-slip boundary condition with a vanishing granular temperature at the boundary yielded a current head reaching 15% longer runout compared to the Jenkins condition. As a result, the central plume was 4% lower. Changes in boundary condition thus do not influence much the stratospheric load.

The far vertical boundary is a free slip wall with respect to the fluid and a no slip wall with respect to the particles. This condition was chosen instead of the more usual (e.g., Valentine and Sweeney, 2018) outflow boundary because the initial atmosphere stratification caused instabilities at that outflow boundary. As a result, runs were stopped when flows approached the distal vertical boundary to avoid their artificial verticalization. The upper boundary conditions are P_f=5.475 kPa, k_t=0.01 J/kg, ε_t=0.1 J/kg s, and a granular temperature of 0.01 m^2/s^2 when particles are present. The vent was 200-m wide and located on the caldera rim at 4.3 km from the central axis (Fig. 1C). Gas and particles were injected vertically at 1300 K. A temperature of 1300 K corresponds to the low range of the inferred temperatures of the basaltic andesite erupted by Okmok volcano in 2008 (Larsen et al. 2013). This parameter was not varied as its effect on column collapse and PDC generation is subordinate to that of mass flux at the vent (Todesco et al., 2002; Todesco et al., 2006). A range of mass fluxes was generated by changing the injection speeds between 166 and 231 m/s and the particle concentration, ε_b, between 1.5 and 4 vol% (Table 1). The choices of speed and ε_b were the same as Dufek and Bergantz (2007a) so that the resulting mass fluxes spanned from buoyant plumes to collapsing columns.

Table 1: *Run parameters. M is the number of solid phases, ε_b is the total particle volume fraction, the flux is that of the solid phases, Volume corresponds to the cumulative amount of erupted solids, DRE stands for Dense Rock Equivalent, and S is the scalar tracking the injected gas (y=present, n=not present).*

Run	*M*	ε_b %	Vent speed m/s	Flux m^3/s	Flux kg/s	Emission duration s	End time s	Volume km^3	Volume DRE km^3	*S*
5 [a]	3	2	173	1.9×10^7	3.5×10^{10}	389	389	7.4	5.5	n
5 stop	3	2	173	1.9×10^7	3.5×10^{10}	100	260	1.9	1.4	n
6	3	0.15	231	1.9×10^6	3.5×10^9	100	189	0.2	0.1	n
7	3	0.5	170	4.7×10^6	8.6×10^9	100	- [d]	- [d]	- [d]	n
	3	0.15	231	1.9×10^6	3.5×10^9	230	330	0.7	0.5	n
7 stop	3	0.5	170	4.7×10^6	8.6×10^9	100	400	0.5	0.3	n
8	1	4	206	4.6×10^7	9.1×10^{10}	227	227	10.4	8.3	n
8 stop	1	4	206	4.6×10^7	9.1×10^{10}	100	201	4.6	3.7	n
9	1	0.5	170	4.7×10^6	9.4×10^9	217	217	1.0	0.8	n
9 stop	1	0.5	170	4.7×10^6	9.4×10^9	100	216	0.5	0.4	n
10	1	3	190	3.1×10^7	6.3×10^{10}	111	111	3.5	2.8	n
11	1	1.5	166 [b]	1.4×10^7	2.8×10^{10}	759	759	10.5	8.4	y
12	1	2	173	1.9×10^7	3.8×10^{10}	105	105	2.0	1.6	y
13	1	2	173 [c]	1.9×10^7	3.8×10^{10}	611	611	11.6	9.3	y

[a] also performed with one solid phase and an algebraic granular equation.
[b] Vent speed was 176 m/s between 108 and 181 s, and 156 m/s between 181 and 240 s.
[c] Vent speed was 163 m/s between 100 and 150 s.
[d] injection conditions changed after 100 s (see following row).

The characteristics of the solid phases are mostly based on the deposit componentry and size distribution (Burgisser 2005). Runs with three solid phases had injections of equal volume fractions of particles of 2000, 1500, and 2000 kg/m^3 with diameters of 2, 0.2, and 0.02 mm, respectively. Assuming, like Burgisser (2005), densities of 1000 kg/m^3 for scoria, 2500 kg/m^3 for lithics and crystals, and 2000 kg/m^3 for glass, the density of the 0.2-mm solid phase corresponds to the observed componentry dominated by crystals and glass. The density of the 0.2-mm solid phase is composed, as observed, of a third of lithics and the rest of scoria. Although the observed componentry of the coarsest fraction is dominated by scoria, we decided to use a density for the 2-mm solid phase that would correspond to a third of scoria and the rest of lithics. For simplicity, runs with a single solid phase had 0.2-mm particles of 2000 kg/m^3. These choices will be shown a posteriori to have a negligible influence on the quantification of the stratospheric loading.

In some runs (7, 11, and 13), collision between sedimenting and rising parts of the fountaining jet caused transient high particle concentrations with very large granular temperatures and solid pressures. The solid pressures caused vanishing time steps that hindered run progression, sometimes stopping it. Continuing such calculations caused the sudden ejection of small (one cell wide) vertical jets of material at high velocities that rapidly dispersed before reaching the tropopause. This behavior was avoided by restarting runs a few seconds before the collision with inlet velocities 10 m/s above or below the base value during <10 s before returning to the original injection velocities.

An implementation issue in most runs caused an error of the value of μ_g of <20% at the coldest

temperature (-57 °C), of 0% at 0 °C, and of <33% at the highest temperature (1027 °C). Duplicating a representative run with a corrected μ_g indicated that this discrepancy altered neither the eruptive dynamics, nor the stratospheric loading. The energy cost of recalculating all runs with a corrected μ_g was deemed too large for the resulting minor gain of knowledge.

2.3. Quantifying stratospheric injection

The efficiency of stratospheric injection was measured by mass balance. The most straightforward way to estimate stratospheric sulfur loading should be to track the volume fraction of gas reaching heights greater than that of the 11 km-high tropopause. Unfortunately, two factors complicate the balance. The plume often escaped from the computational domain at the top boundary at 20 km, making the system open. The second factor was that the injected gas mixed (and reheated) the ambient air. Let M_g^{inj} and M_s^{inj} be the respective masses of injected gas and solids. They are the sum of three components; the respective masses of gas and solids within the computational domain and below 11 km, M_g^b and M_s^b, plus the respective masses of gas and solids within the domain and above 11 km, M_g^a and M_s^a, plus the respective masses of gas and solids lost at the top boundary, M_g^l and M_s^l. As the particle phases have different densities and the injection speed varied in some runs, the mass of solids injected at the vent inlet was given by

$$M_s^{inj} = A_v(1-\varepsilon_g)\rho_b \int \boldsymbol{v}_s(t)dt \tag{8}$$

where A_v=5.5 km^2 is the vent area and ρ_b is the bulk density. Summing the solid mass conservation equations (Eq. 1b) yields expressions for ρ_b and the bulk velocity, v_b, as a function of the sum of all particle fractions, ε_b. As it was assumed that ε_1=ε_2=ε_3=ε_b/3 and v_1=v_2=v_3 at the vent, the bulk density is:

$$\rho_b = \frac{1}{3}\sum \rho_m \tag{9}$$

and the bulk velocity is:

$$v_b = \sum \frac{1/3\rho_m}{\rho_b} v_m = v_m \tag{10}$$

The bulk density is 1833 kg/m^3 when there are three solid phases and 2000 kg/m^3 when there is only one.

To avoid the added uncertainty of mass loss at the top boundary, the fraction of stratospheric solids, F_s, can be calculated as

$$F_s = \frac{M_s^{inj} - M_s^b}{M_s^{inj}} \tag{11}$$

with

$$M_s^b = \sum_{cell}[\pi(r_1^2 - r_2^2)h\sum_M \varepsilon_m\rho_m] \tag{12}$$

where h is the height of the computational cell, r_1 is the radial coordinate of its proximal edge, and r_2 is the radial coordinate of its distal edge.

The fraction of volcanic gas injected into the stratosphere, F_g, could be calculated similarly to F_s (see Eq. 12). Although the injected mass of gas given by:

$$M_g^{inj} = A_v\varepsilon_g\rho_g \int \boldsymbol{v}_g(t)dt \tag{13}$$

is exact, the miscibility of the injected gas with the resident atmosphere leads to an inaccurate estimate of M_g^b using that method (errors of up to 20% of F_g occur at the beginning of the simulation, when M_g^a=M_g^l=0). To minimize such a discrepancy, F_g was instead estimated by:

$$F_g = \frac{M_g^{inj} l + M_g^a}{M_g^{inj}(1+l)} \quad (14)$$

where the mass loss, l, was estimated from the solid mass balance:

$$l = \frac{M_s^l}{M_s^{inj}} = \frac{M_s^{inj} - M_s^a - M_s^b}{M_s^{inj}} \quad (15)$$

Air entrainment was taken into account when calculating the mass of injected gas:

$$M_g^a = \sum_{cell} \pi (r_1^2 - r_2^2) h \varepsilon_g \rho_g S \quad (16)$$

where S was either a scalar advected with the injected gas, or was given by the proxy $S^{-1} = 10^{-4}\left(1300 - T_g\right)^2 + 0.0569\left(1300 - T_g\right) + 1$ when runs did not include the transport of S. The proxy relationship was determined by correlating S and T_g in a run with a scalar (Supplementary Fig. SI1). The relationship between S and T_g is not linear and has some dispersion because $\kappa_g \neq 0$.

3. Results

Ideally, the fraction of solids reaching the stratosphere should equal the fraction of gas reaching the atmosphere when particles travel at the same velocity as that of the gas. This is not necessarily true in our runs because gas and particles are not fully coupled. Leaving the dense part of the PDC aside, the greater decoupling is seen at the edge of the plumes for the coarsest particles, which then leave the cloud and free fall in the surrounding atmosphere. The decoupling between gas and most particles is, however, weak. Within the stratospheric part of the cloud, for instance, the finer particles have typically velocity magnitudes within <1% of that of the gas.

Figure 2 shows the fraction of solids reaching the stratosphere, F_s, vs. the fraction of gas reaching the atmosphere, F_g, for several representative runs. There is a significant degree of mismatch between F_s and F_g. This mismatch is not due to particle decoupling but it is linked to the ways F_g was estimated. First, air entrainment and mixing within the plume causes a diffusion of the injected gas as tracked by a scalar S (see Methods). The approximation created by discretizing the computational domain into cells results in numerical diffusion that increases as the plume rises because computational cells are larger at high altitude (Fig. 1C). Second, in runs where S was not calculated, T_g was used as a proxy to track the degree of such mixing. This adds additional imprecision because the correlation between S and T_g is not perfect (the heated resident atmosphere is then undistinguishable from the injected gas, see Methods). The resulting discrepancies on F_g are mostly <50% but can reach 350%. Thus, the fraction of solids reaching the stratosphere, F_s, which does not suffer from these imprecisions, was used to track stratospheric loading.

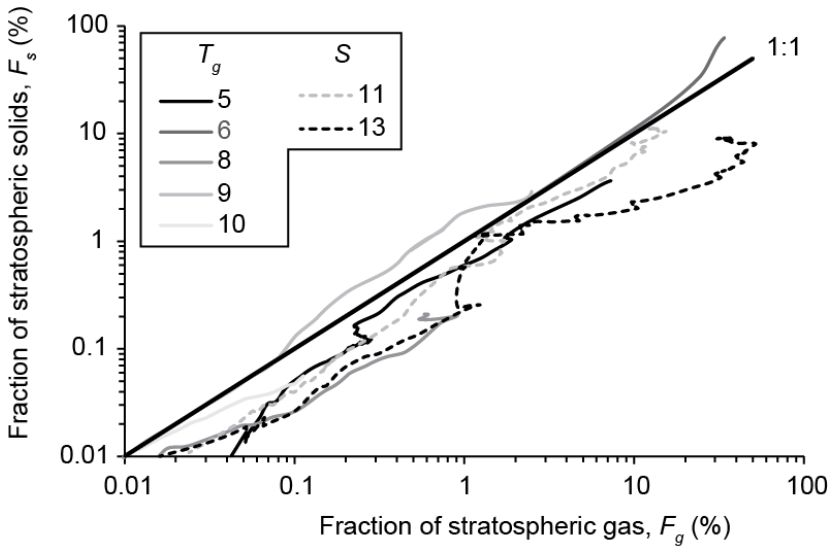

***Figure 2**: Fraction of solids injected into the stratosphere (F_s) vs. fraction of volcanic gas injected into the stratosphere (F_g). Dashed lines indicate runs where F_g was estimated using a gas tracking scalar, S, and solid lines indicate runs where F_g was estimated using gas temperature, T_g. The overall underestimation of F_g compared to F_s is chiefly due to numerical diffusion, gas–particle decoupling playing only a minor role.*

For energy efficiency, most long duration runs were carried out with one particle size instead of three. As the bulk density of the polydisperse runs (1833 kg/m^3) differs from that of the monodisperse run (2000 kg/m^3), the sensitivity test of the stratospheric load to differences in particle sizes and densities was done with the same volume flux but slightly different mass fluxes. Similarly, the total amount of expelled material will be given in km^3 DRE instead of km^3 to ease the comparison between poly- and mono-disperse runs. Overall, the respective PDC runouts differ little and co-ignimbrite clouds have similar shapes at any given time. Figure 3 shows the evolution of F_s for two runs each carried out with one and three particles sizes, respectively. Both evolutions remain close to each other, their F_s values differing by less than 3%. This is because the level of decoupling of the particle motion from the gas motion is low in the buoyant parts of the plumes, leading to a weak segregation of sizes within the co-ignimbrite clouds. Runs were thus considered together regardless of their number of particle sizes.

Mass eruption rate was varied between 3.5×10^9 and 9.1×10^{10} kg/s (Table 1). This free parameter can be constrained in two ways. First, as expected from plume density evolution due to air entrainment (Bursik and Woods 1991), low mass flux should yield a buoyant plume with no PDC. Conversely, high mass flux should yield plume collapse and fountaining that both feed PDCs. In the case of the fixed vent geometry used to simulate the Okmok II eruption, our results suggest that the boundary between buoyant plume and fountain collapse is between 3.5×10^9 and 8.6×10^9 kg/s. A minimum of ~6×10^9 kg/s is thus necessary to account for the thick PDC deposits covering Umnak Island (Fig. 1A).

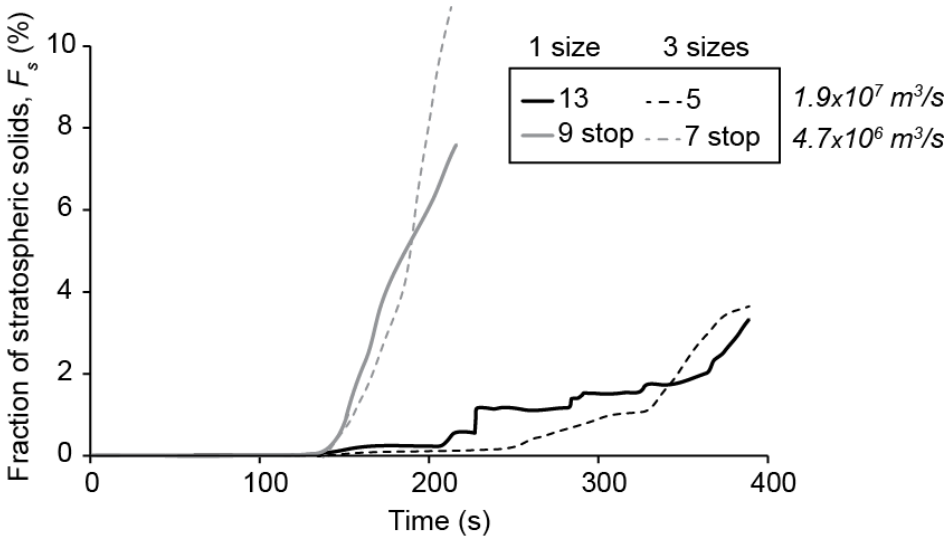

***Figure 3**: Temporal evolution of the fraction of solids injected into the stratosphere (F_s) for runs with one particle size (solid lines) and three particle sizes (dashed lines), respectively. Runs have the same volume flux (in italics) regardless of the number of particle sizes, but slightly different mass fluxes (see text). Black lines are runs continuously emitting ejecta and gray lines are runs that are stopped from emitting after 100 s.*

The second constraint on mass flux is the PDC runout, which was observed to be located at ~29 km from the caldera center in the SW direction (Fig. 1B, Burgisser, 2005). Thick, massive PDC deposits were found up to ~22 km from the caldera center, past two successive hills. Thin, stratified deposits from dilute parts of the PDC were found on the upper slopes of these two first hills. Only thin stratified deposits were found further afield, from ~24.5 km to ~29 km, suggesting deposition from dilute PDC and/or settling co-ignimbrite clouds. Runs with PDC reaching past 29 km were thus deemed to have too long a runout whereas runs producing PDC unable to reach 22 km had too short a runout. A more detailed criterion of runout match with the observed deposits was tentatively applied by defining that $\varepsilon_m \rho_m$ values >100 kg/m^3 in the cells closest to the ground correspond to thick, massive deposits, whereas lower values correspond to thin, stratified deposits. Due to its weakly constrained nature and the large size of the computational cells, this criterion was simply considered as an additional measure used alongside the more robust criterion of runout distance.

Runouts change with time in complex ways. For instance, all runs with mass fluxes >10^{10} kg/s had similar runouts of 15-16 km at 110 s (i.e. they just reached the first hill). Runs with mass fluxes <10^{10} kg/s had much shorter runouts of 11-12 km at that same time. This incremental behavior is due to proximal fountain collapse dynamics, which dictates how much of the momentum of the collapsing material is redirected into horizontal propagation. More distally (and thus after 110 s), the speed of the PDC head strongly controls the runout because of the topographic barriers made by the successive hills. PDC heads with high speeds, such as that of run 8, are able to jump from the first to the second hill, skipping the valley in between, which considerably increases the runout.

Considering that the minimum volume estimate of the Okmok II caldera-forming phase is ~14 km^3 DRE, a successfully matching run should reach 22–29 km after having expelled that amount of material. Unfortunately, this distance seems to be reached for the low end of the explored mass fluxes, which need long durations to reach a given expelled mass. For energy efficiency, only three attempts

have been done to simulate runs expelling >8 km^3 DRE. The highest flux, 9.1×10^{10} kg/s, reached past 29 km at 7.9 km^3 DRE, which suggests that the ideal flux is lower than that value. The two other runs reached ~28 km at 8.3 km^3 DRE of ejecta expelled at 2.8×10^{10} kg/s and 29 km at 9.3 km^3 DRE of ejecta expelled at 3.8×10^{10} kg/s, respectively. This suggests that both runs would have moderately longer runouts than that observed after erupting 14 km^3 DRE. Another measure that leads to the same conclusion is that thick deposits ($\varepsilon_m\rho_m$ > 100 kg/m^3 near the ground) accumulate between the third and fourth hill when >6.6 km^3 DRE are erupted at 2.8×10^{10} kg/s and >8.8 km^3 DRE are erupted at 3.8×10^{10} kg/s.

The range of mass flux fulfilling the combined constraints of fountaining columns producing PDC with runouts similar to those observed is thus between 8.6×10^9 kg/s and 2.8×10^{10} kg/s (or ~10^{10} kg/s for short). As explored below, the natural ejection speed and bulk density are unlikely to be perfectly steady over the eruption duration, so this level of precision at a constant mass flux was deemed sufficient.

Figure 4 shows the stratospheric loading for six PDC-generating runs and one buoyant run as a function of the erupted volume. In all runs with runouts matching that observed, the first part of the erupted material to reach the stratosphere is systematically the central plume formed by the axial convergence of the pyroclastic material flowing from the ring vent towards the center. The central plume is not sustained for long, as it collapses back on itself mid-height at an altitude of ~10–11 km, stopping the stratospheric injection. Overall, the central plume is able to inject 0.1–1% of erupted material above the tropopause. The next pulses of stratospheric injection are caused by the arrival of up to three successive co-ignimbrite clouds issued from the main body of the PDC. These successive clouds inject each an additional few percent of material above the tropopause, bringing the cumulative amount to <12%.

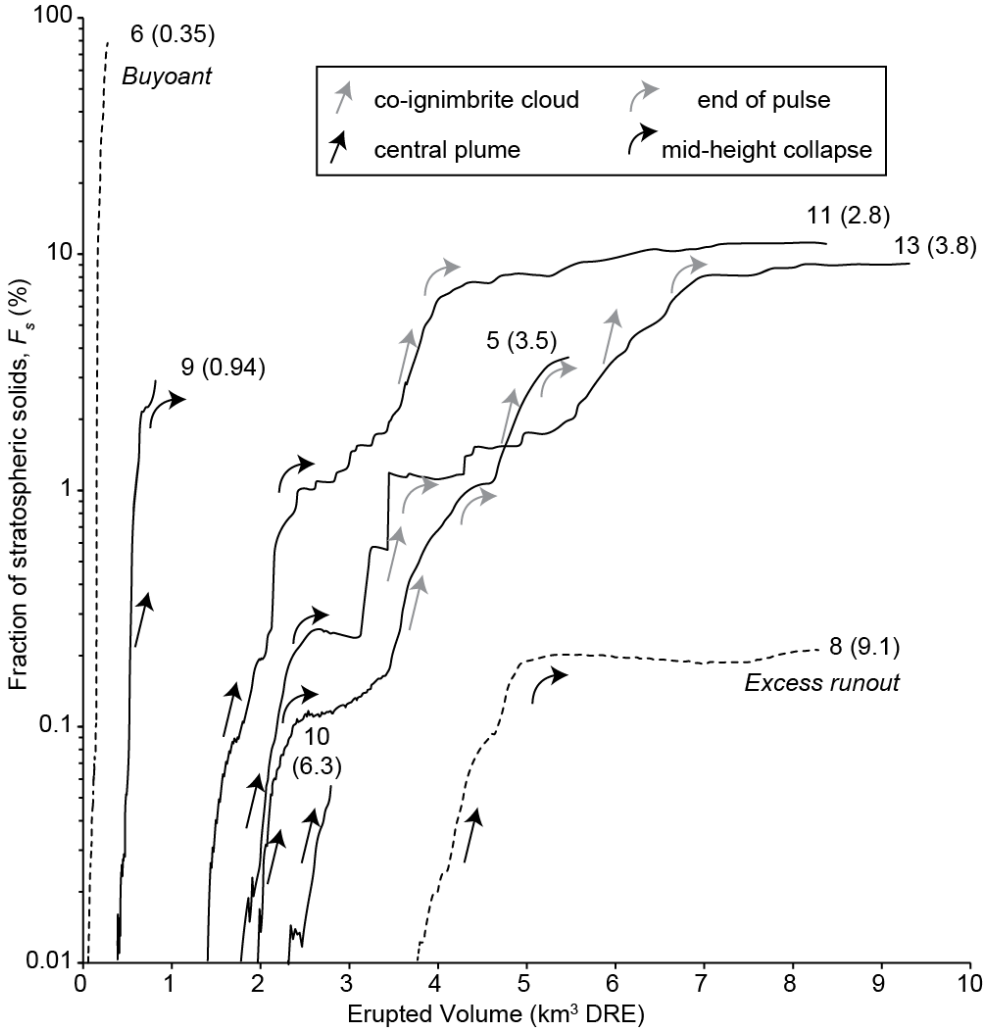

Figure 4*: Fraction of solids injected into the stratosphere (F_s) as a function of erupted volume. Labels indicate run number with the mass flux in parenthesis ($\times 10^{10}$ kg/m^3). Dashed lines represent runs that either did not produce PDC (Buoyant) or had PDC runout far exceeding that observed (Excess runout) and solid lines are PDC-generating runs with plausible runouts. Arrows indicate the underlying reason for the curve evolution (see text for more details).*

The reasons behind co-ignimbrite cloud lift-off are multiple. The first cloud of run 5, for instance, is generated at the apex of the vent because of a favorable configuration of the velocity field generated by air entrainment towards the central plume (Fig. 5). Many clouds are linked to interactions with the hills; the second cloud of run 5 is generated by the PDC head encountering the third hill (Fig. 5). These topographic reliefs cause well-known albeit complex dynamics. For instance, the first cloud of run 13 is generated by the PDC going from a supercritical flow regime above the second hill to a subcritical flow regime when expanding into the ensuing valley. This incipient co-ignimbrite cloud is then fed by more material lifting off as a result of the deceleration caused by the encounter with the third hill. Another cloud-generating mechanism is due to the fact that runs 11 and 13 emit enough material to fill the caldera with fresh, loose deposits. These deposits are constantly remobilized by the arrival of new material, such that, after 400–500 s, this constant reworking causes gargle dynamics (Valentine and Cole 2021). The PDC flowing out of the caldera is affected by such

gargling because it is fed by a thick sheet of dense material partially issued from the overflowing of the caldera. This enhances the generation of a series of small co-ignimbrite clouds that merge when ascending towards the stratosphere.

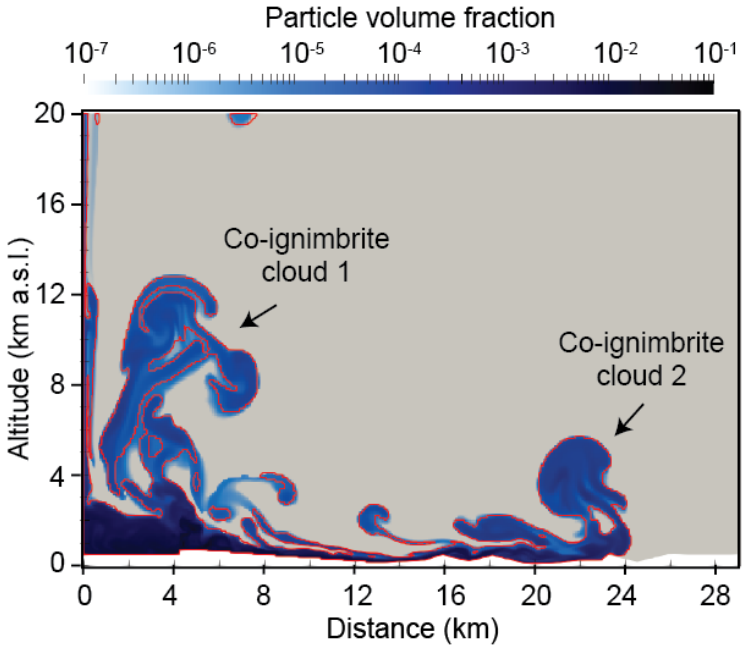

***Figure 5**: Model output example. Particle volume fraction of the 0.02 mm size fraction of run 5 at 259 s. Red curves outline regions where the gas is above background temperature (>12 °C) and the background atmosphere is shown in grey.*

The end of the eruption is likely to send additional material at high altitude by lift-off of the most dilute parts of the slowed down PDC. Figure 6 shows the difference in stratospheric loading between runs in which emission stopped at 100 s and runs where the emission continued beyond 100 s at the same rate. When the eruption stops being fed, the subsequent lift-off of the co-ignimbrite clouds and the most dilute parts of the PDC increases F_s by ~0.4 log unit (a factor 2.5).

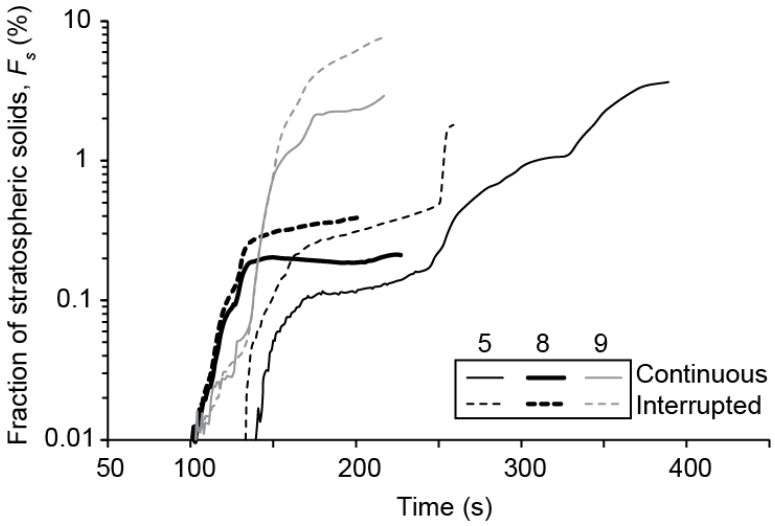

***Figure 6**: Temporal evolution of the fraction of solids injected into the stratosphere (F_s) for runs continuously emitting ejecta (solid lines) and runs stopping emitting after 100 s (dashed lines), respectively. Labels are run number.*

Our runs did not reach the full 14 km^3 DRE of erupted material. However, the runs having emitted ~9 km^3 DRE can outline the most likely scenario of the eruptive dynamics at high altitude. After a first pulse coming from the central plume, most of the stratospheric injection is due to a succession of up to three pulses of co-ignimbrite material issued from the main body of the PDC. The final pulse is due to the PDC head lift-off at the end of the eruption. We thus expect a total injection of at least 2.5% and at most 25% of the ejecta into the stratosphere if the mass flux is steady. Assuming a minimum total erupted volume of 14 km^3 DRE, this corresponds to 0.35–3.5 km^3 DRE of stratospheric material. A more likely total erupted volume of 29 km^3 DRE (Burgisser, 2005; Peccia et al., 2023) yields 0.73–7.3 km^3 DRE of stratospheric material

We used the same two runs having emitted ~9 km^3 DRE to extract velocity profiles above each of the three first hills, at the locations indicated on Fig. 1B. These locations correspond to stratified deposits sampled by Burgisser (2005), who used the corresponding granulometric information to estimate PDC horizontal speed assuming deposition from the dilute part of the current. We calculated the norm of the gas velocity using the convention of positive values indicating horizontal velocities away from the caldera and negative values indicating horizontal velocities towards the caldera. Cells with no particles (ε_m=0) were not included. Figure 7 shows complex gas speed spatial distributions that reach ~150 m/s near Hill 1, ~100 m/s near Hill 2, and ~50 m/s near Hill 3. For each of the 6 profiles, we averaged the gas velocity and the gas root-mean-square velocity in cells having positive speeds as well as dilute conditions (Table 2).

Table 2: *Averaged dynamic parameters of the 3 locations shown on Fig. 1B. RMS stands for root-mean-square gas velocity, avg stands for average, and d is particle median diameter.*

Location	RMS speed [a] m/s	PDC speed [a] m/s	d [a] mm	Run 11 Avg speed m/s	Run 13 Avg speed m/s	Run 11 Avg speed/RMS	Run 13 Avg speed/RMS
L1, Hill1	12.5	50	3.0	54	127	184	31
L2, Hill 2	10.5	42	2.5	90	74	967	7
L3, Hill 3	9	36	1.7	20	20	781	208

[a] Values from Burgisser (2005)

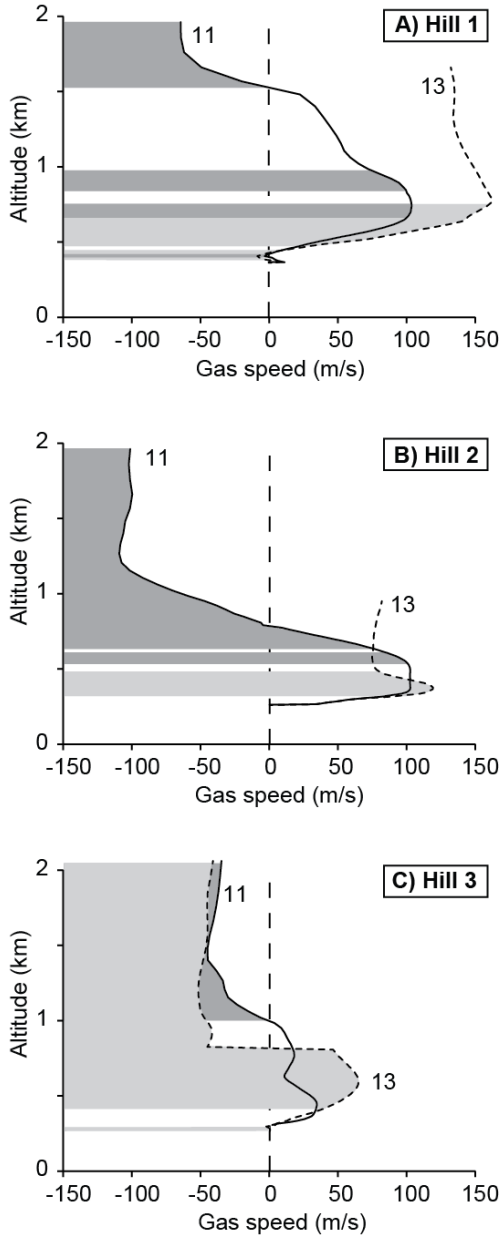

***Figure** 7: Gas velocity magnitude as a function of altitude a.s.l. for three locations. Negative speeds indicate flow towards the caldera and positive speeds indicate flow away from the caldera. Labels indicate run number, and grey horizontal bands indicate where the PDC is dense or backflows towards the caldera. Profiles are shown only at heights where particles are present. A) Location L1 near Hill 1. B) Location L2 near Hill 2. C) Location L3 near Hill 3.*

Even minor oscillations of the eruption rate are likely to cross the transition between buoyant and collapsing eruptive columns. Such oscillation could generate a transitory plume phase during the PDC-dominated eruption, increasing the stratospheric loading, F_s. Figure 8 shows the evolution of F_s for a run starting in the column collapse regime with a flux of 8.6×10^9 kg/s for the first 100 s before switching to the buoyant regime with a flux of 3.5×10^9 kg/s. For comparison, the F_s evolutions of a buoyant run steadily emitting 3.5×10^9 kg/s of ejecta and of a run stopping emitting after 100 s are also shown on Fig. 8. Like in the case of a purely buoyant plume, the transitioning run reaches large values F_s of >50%. Taking into account that the new buoyant plume emitted at 100 s takes an additional ~100 s to reach the tropopause, the rate of increase of F_s is less pronounced when the mass flux leading to buoyancy is preceded by column collapse. Interestingly, the run that stops emitting after 100 s also yields a significant stratospheric loading (50% of the 0.34 km^3 DRE injected at the end of the run) by lift-off of the co-ignimbrite clouds.

Finally, run 12 tested the influence of the shape of the caldera by assuming a filled caldera with a floor flush with the rim. The comparison after 105 s of eruption with a run of identical conditions

but with a depressed caldera floor (run 13) yields minor differences in vortex shapes, identical PDC runouts, and <200 m in central plume height (Supplementary Fig. SI2 in the Online Resource). The uncertainty in pre-eruptive caldera shape has thus a limited impact on the overall dynamics controlling stratospheric loading. A further comparison of F_s values was not attempted owing to the much longer run durations that it would have required.

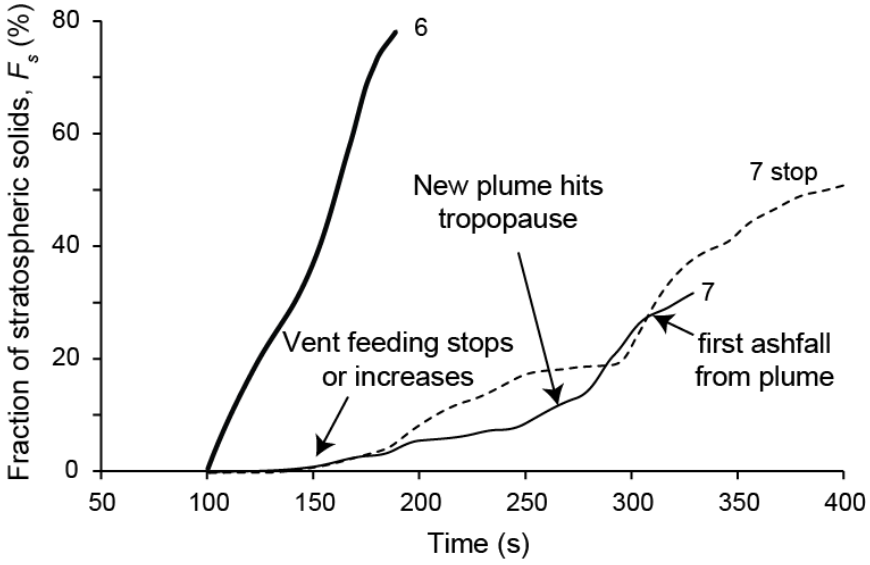

***Figure 8**: Temporal evolution of the fraction of solids injected into the stratosphere (F_s) for a buoyant run (6), a PDC-generating run stopping emitting after 100 s (7 stop), and a PDC-generating run increasing the emission rate after 100 s to become buoyant (7).*

4. Discussion

Our results show that co-ignimbrite clouds occur in pulses rather than in a continuous fashion. This is easily understandable for clouds generated from the body and head of the PDC flowing out of the caldera because of the encounters with complex topography. It is perhaps more surprising for the central plume because it is fed continuously by the convergence of the collapsing fountain atop the ring vent. The pulsatory nature of the central plume is explained by the appearance of one region above which the plume is positively buoyant and below which it is negatively buoyant (Valentine and Cole 2021). The appearance of a neutrally buoyant point is explained by a reduction of the bulk density of the ascending mixture of gas and particles caused by the interaction with the atmosphere. When this mixture density deceases below that of the surrounding atmosphere before running out of ascending momentum, it rises as a buoyant plume instead of collapsing to the ground (Bursik and Woods 1991).

Our simulations suggest an average mass flux of ~10^{10} kg/s. This estimate is within an order of magnitude of the maximum flux of 1.4×10^{11} kg/s estimated by Burgisser (2005) from the granulometry of stratified deposits and assuming instantaneous deposition. This coarse estimate assumes that speed estimates near the shore (60 m/s) are representative of the average current velocity, and deduces the average mass flux if the full volume of on land deposits were emplaced at that rate. Two of the Burgisser (2005) estimates (50, 42, and 36 m/s) are within the range of average gas velocity at each location (54–127, 74–90, and 20 m/s), respectively. Despite that longer runs should be performed to compensate that our runs emit only 2/3 of the total PDC volume, this overlap

is most likely fortuitous because one key assumption of the Burgisser (2005) estimates is that the root-mean-square gas velocity is exactly 4 times larger than the mean PDC speed. Our runs, however, suggest a wide variation of this ratio between 7 and 967 (Table 2), which casts a doubt on the accuracy of using a single ratio established for particle-free, fully turbulent flows. This is confirmed by the fact that dilute conditions are only achieved at certain ranges of height within the current (Fig. 7). Linking deposits characteristics to PDC dynamics is a challenging task that often requires the addition of Lagrangian particles (e.g., Dufek and Bergantz, 2007a), which was not attempted in our study. Hence, our simulations cannot be directly compared to dynamical parameter estimates stemming from deposits because the particle size of our longer runs, 0.2 mm, is one order of magnitude above that of the deposits (Table 2). A meaningful comparison would need runs with more particle sizes and smaller grid size near the topography.

The simulation ignored PDC travel over water because the cross section focused on the interaction between the PDC and the series of hills on the SW of the caldera. Stratified deposits from the dilute parts of the Okmok II PDC were found on the neighboring island of Unalaska, suggesting that the PDCs crossed the 8-km wide strait between the two islands (Burgisser 2005). Overwater travelling causes particle loss, which dilutes the PDC and favors the generation of co-ignimbrite clouds (Dufek and Bergantz, 2007a; Dufek and Bergantz, 2007b). While this seems an incentive to address overwater travel, the analysis of the deposits also showed that the dynamics of the crossing was rapidly and significantly affected by large pumice rafts that created a skin able to support bouncing of lithics that would otherwise sink (Burgisser 2005). The additional generation of offshore co-ignimbrite clouds cannot thus be excluded but the inhibiting role of pumice rafts probably minimized such sources of stratospheric injection. Addressing that issue was deemed to exceed the predictive capability of our PDC modeling.

A fluctuating emission rate or an efficient final lift-off could increase the loading we estimated from a steady mass flux at the vent, but it is unlikely. A buoyant plume would have left recognizable fall deposits interbedded with the massive deposits, which is not seen of the field (Burgisser, 2005; Larsen et al., 2007). Signs of fall deposits would also be present within or atop the stratified deposits found on the topographic highs of Umnak, and within those blanketing Unalaska. Field observations are thus not compatible with any significant fallout episode. The same reasoning applies to a massive lift-off of co-ignimbrite clouds at the end of the eruption. The flow path we simulated crosses a rugged part of the topography surrounding the caldera. Other reliefs, such as Idak plateau that covers the NE end of Umnak island, could generate co-ignimbrite clouds at various locations, but some flow directions, such as towards the SE, lack topography. These considerations point to 25% being a most likely upper estimate of F_s.

We may venture into a more speculative estimate to address an extreme scenario in which buoyant plume phases occur during the eruption, but the related fallout ash is swept by the subsequent PDC phase and mixes with it such that no trace of the plume is left in the deposits. Examination of runs where small co-ignimbrite clouds collapse back into the underlying current suggest that the main PDC phase has to last more than 400 s to entrain fully the sedimenting material. The buoyant plume phase can last at most 200 s before the main PDC stops being fed (Fig. 8), which would cause a distinct depositional unit when the subsequent current head travels outward to re-establish the PDC. Under perfect timing, at most 8 cycles of alternating PDC–buoyant plumes can fit within the eruption window. As a result, 83% of the material is emitted during the PDC phases while only 13% is emitted during the less energetic plume phases. Considering that a maximum of 25% of the PDC material (see above) and 90% of the plume material (Fig. 8) can reach past the tropopause, this extreme scenario

yields a total of 32% of stratospheric injection. Compared to 25%, this very modest increase of maximum loading does not seem to justify the series of ad-hoc assumptions underlying this scenario.

We thus estimate from Figs. 5 and 6 that, overall, between 2.5 and 25% of the emitted volcanic gas was able to reach the stratosphere. The corresponding stratospheric load of S controls the atmospheric forcing and the climatic response in temperature and precipitation changes (McConnell et al., 2020; Peccia et al., 2023). The sulfur load of the juvenile magma has been determined by the petrologic method, which quantifies the difference between the S contained in melt inclusion and that remaining in the glass, correcting for crystal content (Peccia et al. 2023). This method suggests that ~1500 ppm of sulfur was degassed during the climactic PDC phase of Okmok II. The total amount of juvenile magma emitted by this phase can be obtained from the total volume corrected for the amount of lithics (26 wt%, Burgisser, 2005). Using a total erupted volume of 29 km^3 DRE, Peccia et al. (2023) calculate a total juvenile magma mass of ~4.3×10^{13} kg, which in turn produced a total sulfur load of ~62 Tg S. Thus, 46.5–60.4 Tg of the emitted S remained in the troposphere while 1.6–15.5 Tg S was injected into the stratosphere. This amount of stratospheric S is lower than the 38–48 Tg S inferred previously from source location, ice core sulfate concentrations, and hemispheric depositional asymmetry (McConnell et al., 2020; Pearson et al., 2022), while it is comparable to the 18–22 Tg S inferred from tree ring and speleothem temperature reconstructions and climate model response to S (Peccia et al. 2023). The reader is directed to the work of Peccia et al. (2023) for an in-depth analysis of the inferences that can be drawn from these different results.

5. Conclusions

This work presents results from computational fluid dynamics aimed at estimating the amount of material reaching the stratosphere during the eruption of Okmok II. Axisymmetric, 2D simulations were carried out with the two-phase flow model MFIX-TFM. They modelled the dynamics of the climactic phase of the eruption with several combinations of injection mass flux, emission duration, and topography. Model outputs were constrained by the volume of the deposits and their distribution on the SW of the caldera, where four successive hills caused deposit thickness to vanish progressively. The efficiency of stratospheric injection was measured by mass balance of gas and solids.

Our simulations suggest that an average mass flux of $8.6–28\times10^9$ kg/s is consistent with field observations. Stratospheric (>11 km high) injections occur in pulses rather than in a continuous fashion. The first injection is caused by the convergence of the collapsing fountain atop the ring vent in the center of the caldera that generates a central plume. This central plume is able to inject 0.1–1% of erupted material above the tropopause before collapsing back on itself, stopping the stratospheric injection. The next pulses reaching the stratosphere are successive co-ignimbrite clouds issued from the head and main body of the PDC as it encounters complex topography. They add up to 12% of the erupted material in the stratosphere. Finally, the end of the eruption causes a buoyant lift-off of the co-ignimbrite clouds and the most dilute parts of the PDC, which multiplies the existing injected proportion by a factor 2.5. Our main result is thus that between 2.5 and 25% of the emitted volcanic gas is able to reach the stratosphere if the mass flux at the vent is steady.

A fluctuating emission rate or an efficient final lift-off due to seawater interaction could increase the loading we estimated from a steady mass flux at the vent, but modeling and field constraints suggest that it is unlikely. The strongest field constraint is that a sustained buoyant plume would have left recognizable (and yet absent) fall deposits interbedded with the massive deposits.

The corresponding stratospheric load of S controls the atmospheric forcing and the subsequent climatic response in temperature and precipitation changes. Using a total erupted volume of 29 km^3 DRE and petrological constraints on the amount of S degassed, our study suggests that Okmok II produced a total sulfur load of ~62 Tg, of which 46.5–60.4 Tg remained in the troposphere and 1.6–15.5 Tg was injected into the stratosphere.

Acknowledgments

We thank G. Valentine for helping us identifying gargle dynamics in our simulations and J. Larsen for suggesting exploring alternate pre-eruptive topography.

Funding

This project was partially funded by grant ANR-19-CE31-0007 from Agence Nationale pour la Recherche. The computations presented in this paper were performed using the GRICAD infrastructure (gricad.univ-grenoble-alpes.fr), which is supported by Grenoble research communities.

Statements and Declarations

No ethical question is raised by this study. All authors and co-authors have given their consent to be included in this manuscript. Consent has been given for publishing this manuscript and the authors declare no competing interests.

References

Agrawal K, Loezos PN, Syamlal M, Sundaresan S (2001) The role of meso-scale structures in rapid gas–solid flows. J Fluid Mech 445:. https://doi.org/10.1017/S0022112001005663

Benage MC, Dufek J, Degruyter W, et al (2014) Tying textures of breadcrust bombs to their transport regime and cooling history. J Volcanol Geotherm Res 274:92–107

Benage MC, Dufek J, Mothes PA (2016) Quantifying entrainment in pyroclastic density currents from the Tungurahua eruption, Ecuador: Integrating field proxies with numerical simulations. Geophys Res Lett 43:6932–6941. https://doi.org/10.1002/2016GL069527

Benyahia S (2008) Validation Study of Two Continuum Granular Frictional Flow Theories. Ind Eng Chem Res 47:8926–8932. https://doi.org/10.1021/ie8003557

Benyahia S, Syamlal M, O'Brien TJ (2005) Evaluation of boundary conditions used to model dilute, turbulent gas/solids flows in a pipe. Powder Technol 156:62–72. https://doi.org/10.1016/j.powtec.2005.04.002

Benyahia S, Syamlal M, O'Brien TJ (2007) Study of the ability of multiphase continuum models to predict core-annulus flow. AIChE J 53:2549–2568. https://doi.org/10.1002/aic.11276

Breard ECP, Dufek J, Roche O (2019) Continuum Modeling of Pressure-Balanced and Fluidized Granular Flows in 2-D: Comparison With Glass Bead Experiments and Implications for Concentrated Pyroclastic Density Currents. J Geophys Res Solid Earth 124:5557–5583. https://doi.org/10.1029/2018JB016874

Burgisser A (2005) Physical volcanology of the 2,050 bp caldera-forming eruption of Okmok volcano, Alaska. Bull Volcanol 67:497–525. https://doi.org/10.1007/s00445-004-0391-5

Burgisser A, Bergantz GW (2002) Reconciling pyroclastic flow and surge: the multiphase physics of pyroclastic density currents. Earth Planet Sci Lett 202:405–418

Bursik MI, Woods AW (1991) Buoyant, superbuoyant and collapsing eruption columns. J Volcanol Geotherm Res 45:347–350

Crowe C, Sommerfeld M, Tsuji Y (1997) Multiphase flows with droplets and particles. CRC Press, Boca Raton

Dufek J, Bergantz GW (2007a) Suspended load and bed-load transport of particle-laden gravity currents: the role of particle–bed interaction. Theor Comput Fluid Dyn 21:119–145. https://doi.org/10.1007/s00162-007-0041-6

Dufek J, Bergantz GW (2007b) Dynamics and deposits generated by the Kos Plateau Tuff eruption: Controls of basal particle loss on pyroclastic flow transport. Geochem Geophys Geosystems 8:

Dufek J, Wexler J, Manga M (2009) Transport capacity of pyroclastic density currents: Experiments and models of substrate-flow interaction. J Geophys Res Solid Earth 114:. https://doi.org/10.1029/2008JB006216

Esposti Ongaro T, Komorowski J-C, Legendre Y, Neri A (2020) Modelling pyroclastic density currents from a subplinian eruption at La Soufrière de Guadeloupe (West Indies, France). Bull Volcanol 82:76. https://doi.org/10.1007/s00445-020-01411-6

Garg R, Galvin J, Li T, Pannala S (2010) Documentation of open-source MFIX–DEM software for gas-solids flows. URL Httpsmfix Netl Doe Govdocumentationdemdoc2012-1 PdfAccessed 31 March 2014

Gunn DJ (1978) Transfer of heat or mass to particles in fixed and fluidised beds. Int J Heat Mass Transf 21:467–476. https://doi.org/10.1016/0017-9310(78)90080-7

Jenkins JT (1992) Boundary Conditions for Rapid Granular Flow: Flat, Frictional Walls. J Appl Mech 59:120–127. https://doi.org/10.1115/1.2899416

Larsen JF, Neal C, Schaefer J, et al (2007) Late Pleistocene and Holocene caldera-froming eruptions of Okmok caldera, Aleutian Islands, Alaska. 172:324–364

Larsen JF, Śliwiński MG, Nye C, et al (2013) The 2008 eruption of Okmok Volcano, Alaska: Petrological and geochemical constraints on the subsurface magma plumbing system. J Volcanol Geotherm Res 264:85–106. https://doi.org/10.1016/j.jvolgeores.2013.07.003

Liu Y, Xu T, Liu J (2014) Characteristics of the seasonal variation of the global tropopause revealed by COSMIC/GPS data. Adv Space Res 54:2274–2285. https://doi.org/10.1016/j.asr.2014.08.020

McConnell JR, Sigl M, Plunkett G, et al (2020) Extreme climate after massive eruption of Alaska's Okmok volcano in 43 BCE and effects on the late Roman Republic and Ptolemaic Kingdom. Proc Natl Acad Sci 117:15443–15449. https://doi.org/10.1073/pnas.2002722117

Moitra P, Sonder I, Valentine GA (2020) The role of external water on rapid cooling and fragmentation of magma. Earth Planet Sci Lett 537:116194. https://doi.org/10.1016/j.epsl.2020.116194

National Oceanic and Atmospheric Administration (1976) US Standard Atmosphere

Neri A, Esposti Ongaro T, Menconi G, et al (2007) 4D simulation of explosive eruption dynamics at Vesuvius. Geophys Res Lett 34:

Pearson C, Sigl M, Burke A, et al (2022) Geochemical ice-core constraints on the timing and climatic impact of Aniakchak II (1628 BCE) and Thera (Minoan) volcanic eruptions. PNAS Nexus 1:pgac048. https://doi.org/10.1093/pnasnexus/pgac048

Peccia A, Moussallam Y, Plank T, et al (accepted on Sept 13, 2023) Multi-Parameter Assessment of Stratospheric Sulfur Load from the Okmok II Caldera-Forming Eruption of BCE 43. Geophys Res Lett

Pope SB (2000) Turbulent flows. Cambridge University Press, Cambridge, UK

Sweeney MR, Valentine GA (2017) Impact zone dynamics of dilute mono- and polydisperse jets and their implications for the initial conditions of pyroclastic density currents. Phys Fluids 29:093304. https://doi.org/10.1063/1.5004197

Syamlal M (1998) MFIX documentation numerical technique. EG and G Technical Services of West Virginia, Inc., Morgantown, WV (United States)

Syamlal M, Rogers W, OBrien TJ (1993) MFIX documentation theory guide. USDOE Morgantown Energy Technology Center, WV (United States)

Todesco M, Neri A, Esposti Ongaro T, et al (2002) Pyroclastic flow hazard assessment at Vesuvius (Italy) by using numerical modeling. I. Large-scale dynamics. Bull Volcanol 64:155–177

Todesco M, Neri A, Esposti Ongaro T, et al (2006) Pyroclastic flow dynamics and hazard in a caldera setting: Application to Phlegrean Fields (Italy). Geochem Geophys Geosystems 7:

U.S. Geological Survey EROS Data Center (1999) 7.5-minute Digital Elevation Model (10 meter resolution). U. S. Geological Survey, Sioux Falls, SD

Valentine GA (2020) Initiation of dilute and concentrated pyroclastic currents from collapsing mixtures and origin of their proximal deposits. Bull Volcanol 82:20. https://doi.org/10.1007/s00445-020-1366-x

Valentine GA, Cole MA (2021) Explosive caldera-forming eruptions and debris-filled vents: Gargle dynamics. Geology 49:1240–1244. https://doi.org/10.1130/G48995.1

Valentine GA, Sweeney MR (2018) Compressible Flow Phenomena at Inception of Lateral Density Currents Fed by Collapsing Gas-Particle Mixtures. J Geophys Res Solid Earth 123:1286–1302. https://doi.org/10.1002/2017JB015129

Wen CY, Yu YH (1966) Mechanics of fluidization. Chem Eng Prog Symp Ser 62:100–111

Numerical simulations of the latest caldera-forming eruption of Okmok volcano, Alaska

Alain BURGISSER [1*], Ally PECCIA [2], Terry PLANK [2], Yves MOUSSALLAM [2]

[1] Univ. Grenoble Alpes, Univ. Savoie Mont Blanc, CNRS, IRD, Univ. Gustave Eiffel, ISTerre, 38000 Grenoble, France.

[2] Lamont-Doherty Earth Observatory, Palisades, NY 10964, USA.

* Corresponding author: Phone: (+33) 479 758 705. Email: alain.burgisser@univ-smb.fr

Supplementary Information

This Supplementary Information includes 2 figures (Figs. S1–S2).

Supplementary Figures

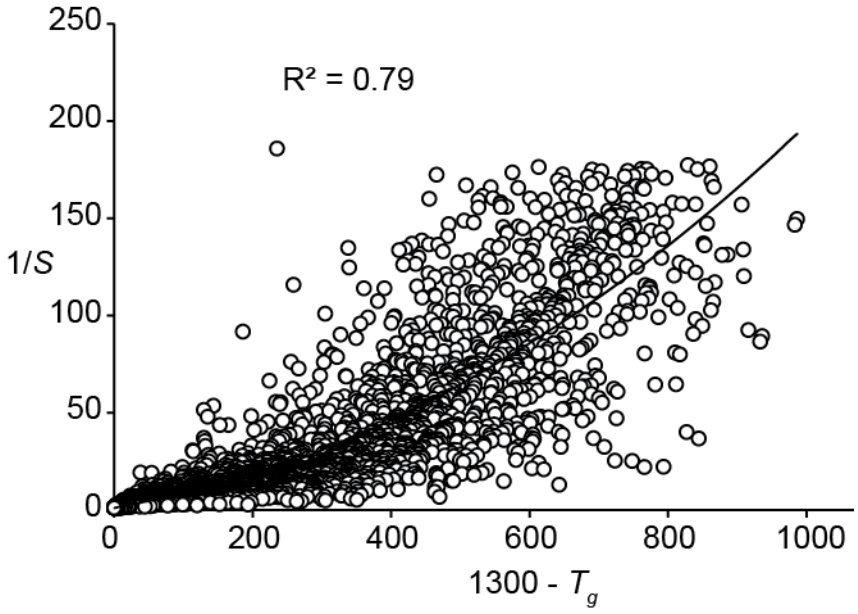

Figure S1: Gas temperature as a function of the inverse of the scalar tracking the injected gas. The solid line is a quadratic regression curve fitted to the data and R^2 is the squared Pearson's correlation coefficient.

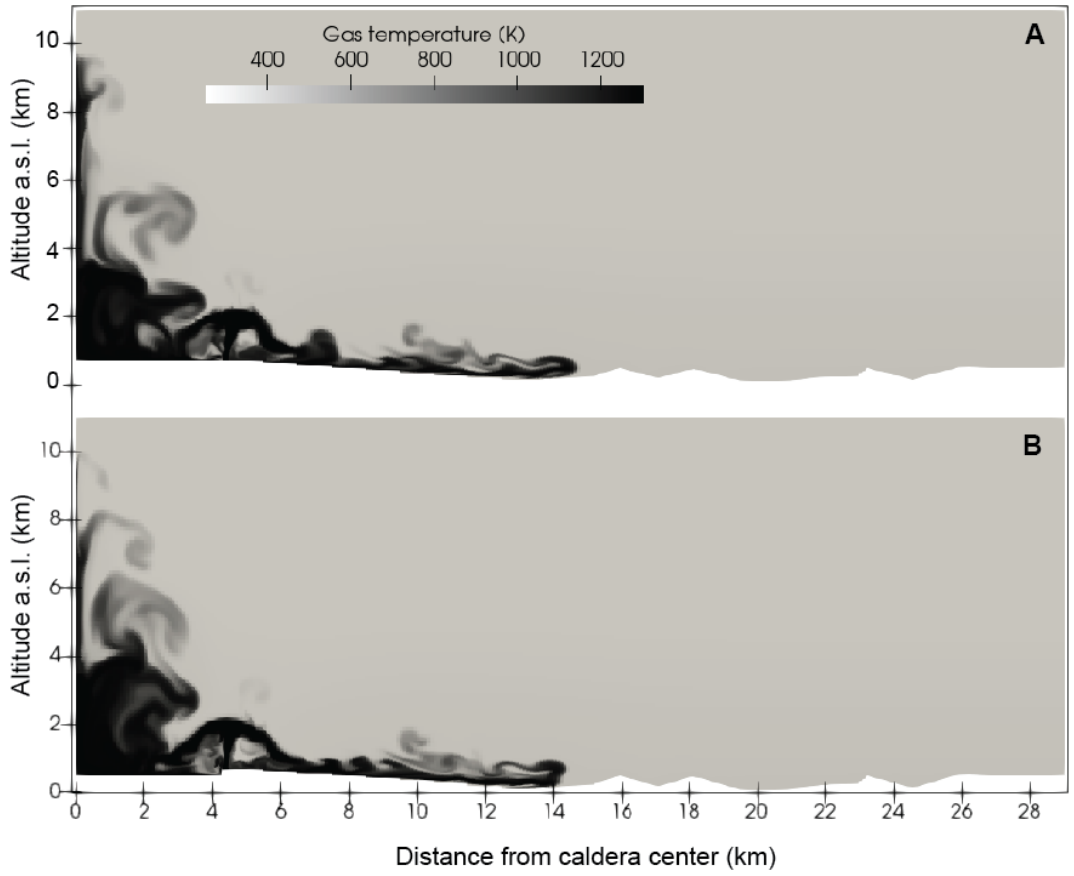

Figure S2: Distribution of gas temperature at 100 s. A) Run 12 with a filled caldera. B) Run 13 with a depressed caldera floor corresponding to the current topography.